Key Points:
- Deformation experiments on Etna basalt and Comiso limestone are performed under confined (50 MPa) and volcanic temperature conditions (up to 1,000 °C)
- Constitutive equations are derived from laboratory data, extrapolated to field conditions, and validated with local seismicity occurrence
- Ductile flow of limestone in the basement can explain the observed deformation pattern of Mt. Etna's eastern flank

Constitutive Laws for Etnean Basement and Edifice Lithologies

Richard R. Bakker[1,2] (iD), Marie E. S. Violay[1,3] (iD), Sergio Vinciguerra[4] (iD), Marco Fazio[5,6] (iD), and Philip M. Benson[5] (iD)

[1]Geological Institute, Structural Geology and Tectonics, ETH Zürich, Zürich, Switzerland, [2]Now at Civil Engineering and Geosciences, Delft University of Technology, Delft, Netherlands, [3]Laboratory of Experimental Rock Mechanics, EPFL, Lausanne, Switzerland, [4]Department of Earth Sciences, University of Turin, Turin, Italy, [5]Rock Mechanics Laboratory, School of Earth and Environmental Sciences, University of Portsmouth, Portsmouth, UK, [6]Abteilung Angewandte Geologie, Geowissenschaftliches Zentrum, Universität Göttingen, Göttingen, Germany

Abstract The mechanical dynamics of volcanic systems can be better understood with detailed knowledge on strength of a volcanic edifice and subsurface. Previous work highlighting this on Mt. Etna has suggested that its carbonate basement could be a significant zone of widespread planar weakness. Here, we report new deformation experiments to better quantify such effects. We measure and compare key deformation parameters using Etna basalt, which is representative of upper edifice lava flows, and Comiso limestone, which is representative of the carbonate basement, under upper crustal conditions. These data are then used to derive empirical constitutive equations describing changes in rocks strength with pressure, temperature, and strain rate. At a constant strain rate of 10^{-5} s^{-1} and an applied confining pressure of 50 MPa, the brittle-to-ductile transitions were observed at 975 °C (Etna basalt) and 350 °C (Comiso limestone). For the basaltic edifice of Mt. Etna, the strength is described with a Mohr-Coulomb failure criterion with $\mu \sim 0.704$, $C = 20$ MPa. For the carbonate basement, strength is best described by a power law-type flow in two regimes: a low-T regime with stress exponent $n \sim 5.4$ and an activation energy $Q \sim 170.6$ kJ/mol and a high-T regime with $n \sim 2.4$ and $Q \sim 293.4$ kJ/mol. We show that extrapolation of these data to Etna's basement predicts a brittle-to-ductile transition that corresponds well with the generally observed trends of the seismogenic zone underneath Mt. Etna. This in turn may be useful for future numerical simulations of volcano-tectonic deformation of Mt. Etna, and other volcanoes with limestone basements.

Plain Language Summary To be able to understand the deformation of volcanoes, such as ground movement and risks of flank collapse, we need to know under what conditions (temperature, stress, and overburden) the rocks either bend (flow) or break inside the volcano. Here we focus on Mt. Etna and study rocks from the edifice (basalt) and the rocks that the volcano is built upon (limestone that crops out at the surface at the town of Comiso, South East Sicily, Italy). We take the rocks to the laboratory where we deform the rocks under various temperature, confining pressure (to simulate overburden) and deformation rates. We then use the laboratory data to build up equations that can be used to figure out how the rocks behave underneath the volcano, at high temperatures and natural deformation speeds (which are a lot slower than in the lab). We check if our equations compare well to natural behavior by comparing with field data (earthquakes), which only happens when rocks break or slide along a fault plane, and not when the rocks are flowing. The equations may be used as input for future studies on the deformation of the volcano.

1. Introduction

The mechanical influence of basement rocks on the deformation of overlying volcanic strata is poorly understood but is likely a key factor for understanding volcanic stability (Poland et al., 2017). Ductile deformation in sedimentary basement rocks has been cited as a cause of volcanic instability without requiring significant magmatic intrusions (e.g., Heap et al., 2015; Poland et al., 2017; van Wyk de Vries & Borgia, 1996; van Wyk de Vries & Francis, 1997). In such cases, the mechanical properties of subvolcanic lithologies may have a prominent effect on the stability of volcanic edifices by initiating a plastic "spreading" of the sub-Etnean basement. In a worst-case scenario this propagates to the overlying edifice, potentially causing the volcano to collapse, even during periods of eruptive quiescence (van Wyk de Vries & Francis, 1997). This may be

particularly of importance for volcanoes with carbonate basements, as carbonate rocks are prone to ductile deformation behavior at relatively low temperatures, easily achieved within a volcanic system (e.g., Bakker et al., 2015; Heap et al., 2013). Known examples of such volcanoes include Merapi in Indonesia (e.g., Chadwick et al., 2007), Vesuvius (e.g., Iacono-Marziano et al., 2009), and Mt. Etna in Italy (e.g., Bakker et al., 2015; Heap et al., 2013; Mollo et al., 2011).

One of the flanks of Mt. Etna is a good example of a large-scale volcanic instability: its eastern edifice (e.g., Borgia et al., 1992; Murray et al., 2018; Palano, 2016; Tibaldi & Groppelli, 2002), which has been linked to its lower basement structure. Etna is a strato-volcano consisting of basaltic cover of cumulative lava flows of 1.5-km-average thickness (maximum of approximately 2.2 km below the summit area tapering to approximately 1 km along the flanks) that overlies a thick sedimentary basement (Branca et al., 2011). This consists of a sequence of sub-Etnean clays (known as the blue clays), resting upon an imbricated sequence of sediments of the Apennine Maghrebian Chain (AMC) such consolidated clays, marly limestones, and quartz-arenitic rocks about 2–3 km thick (Branca et al., 2011; Branca & Ferrara, 2013; Nicolosi et al., 2014; Wiesmaier et al., 2015). These in turn overlie a Mesozoic to Mid-Pleistocene carbonate succession of "Comiso" limestone and dolomite, part of the Hyblean Plateau, the undeformed foreland domain composed of a 25- to 30-km crust (Bakker et al., 2015; Heap et al., 2013; Wiesmaier et al., 2015). This formation is estimated to start 4 km underneath Mt. Etna (Branca et al., 2011; Wiesmaier et al., 2015) and 6 km in the south (Branca et al., 2011; Castagna et al., 2018).

Work to date investigating the deformation and failure mode of these materials includes uniaxial compressive strength (UCS), P wave velocity, and static Youngs modulus on a range of rocks in and around Mt. Etna, such as marly limestones, quartzarenites, dolomitic and radiolaritic limestones, marly clay, and calcarenites (Wiesmaier et al., 2015). However, these data largely report ambient (room) conditions, whereas the deep rheology of the volcano is likely to be significantly altered by high temperatures originating from the volcanic system. A number of studies have therefore run either confined tests or tests at high temperature on specific lithologies found within the suite of Wiesmaier et al. (2015).

Mollo et al. (2011) have investigated the UCS of limestones found within the AMC unit at temperatures up to 800 °C. They found that UCS values are some 90% lower at 800 °C with respect to its room temperature strength due to the dehydroxylation of clay minerals and the decarbonation of calcium carbonate. Although these devolatilization reactions (the primary weakening mechanism) stall when the system becomes buffered by rising levels of reaction product, rock mechanical properties (strength) continues to degrade due to thermal microcracking (Mollo et al., 2012, 2013). However, the vast majority of these data have been obtained without effective stress on the samples (i.e., test with mechanical confinement), which could suppress microcracking behavior, and therefore might not be completely representative of the rheological behavior at "in situ" pressure and temperatures (PT). To address this, recent experiments have shown that such conditions significantly alter the rheological behavior of carbonates belonging to the Etna basement (Bakker et al., 2015). This work noted in particular that the brittle-to-ductile transition (BDT) temperature for Comiso limestone takes place at a lower temperatures then previously measured on limestone from the Hybean foreland (between 500 and 600 °C for Mt. Climiti limestone at a strain rate of 1.5×10^{-5} s^{-1}) using ambient pressure and elevated temperatures (Heap et al., 2013). Moreover, the effects of decarbonation reactions were minimal due to the lack of sufficient permeability to allow free outgassing from the pores at elevated temperatures (Bakker et al., 2015). Recently, Castagna et al. (2018) have shown the effects of thermally induced microcracks and pore fluid pressure on the BDT of Comiso limestone. They conclude that both lead to a decrease the mechanical strength of the lithology and enhance plastic mechanisms, which in turn is qualitatively discussed to causing a more shallow BDT depth.

At shallower levels, Mt. Etna is primarily composed of lava flow basalts. The most common of these is a porphyritic intermediate alkali basalt (Tanguy et al., 1997). Samples from lava flows can be notably heterogeneous due to different cooling rates. As such, some samples can feature an extensive preexisting network of interconnected microcracks. These are interpreted as being of thermal origin, since various physical properties are not affected by further thermal stressing (e.g., Vinciguerra et al., 2005). The stress-induced degradation of the mechanical properties of this lithology has been widely investigated in the laboratory. For example, Heap et al. (2009) show a decrease in the Young's modulus (E) by about 30% (down to 20 GPa) with increasing stress cycles. This behavior was primarily attributed to an increase in the level of crack damage

within the samples. Triaxial compression tests at room temperature show that the faulting process in such a rock is slower than in other crystalline rocks with such crack damage and failure only occurs after the fault zone has completely traversed the sample (Benson et al., 2007). Similar triaxial experiments performed at room temperature show the compressive strength is increased from 291 to 504 MPa at effective confining pressures of 10 to 50 MPa (Heap et al., 2011)

Benson et al. (2012) studied the effects of temperature on the UCS of Etna basalt up to 950 °C. While all tests resulted in brittle failure (defined as a sudden loss of load carrying capacity; Rutter, 1986), they did suggest an onset of ductile behavior above 950 °C. However, these tests were done at variable (cyclic) strain rates that mimic volcano-tectonic behavior. Moreover, they were unable to develop an understanding of the pressure dependence of this rheology due to equipment limitations. This is important, as in order to derive a full understanding of the mechanical behavior of rocks forming the Etna's edifice and its basement at increasing depth and temperature, both the shallow basalt and the deeper carbonates require a strength profile at representative conditions, taking into account pressure, temperature, and strain rate.

In this paper, we present new laboratory data on the rheological properties of the two main end-members, that is, Etna basalt (representing the main upper edifice-building lithology) and Comiso limestone (representing the main lower basement lithology and its deeper roots) based on a new suite of high-pressure/high-temperature experiments. Specifically, for Comiso limestone, this work builds upon the constant strain rate experiments presented earlier (Bakker et al., 2015). The new experiments focus on the plastic effects observed at temperatures above the BDT at a strain rate of 10^{-5} s^{-1} and 50 MPa of confining pressure. With this we aim to expand our understanding of rheological properties under subvolcanic PT conditions. We use constant strain rate experiments to evaluate the approximate temperature ranges for various deformation mechanisms (for which we present new data on Etna basalt and use the results of Bakker et al., 2015, for Comiso limestone). We perform additional experiments to further constrain the rheological behavior at elevated PT conditions: triaxial friction tests on both rock types for the low-temperature domain and strain rate stepping tests for the high-temperature domain for Comiso limestone. From these data and with the help of literature data to take in account of the complexity of the sub-Etnean basement (particularly the AMC), an empirical constitutive law is formulated, which enables extrapolation to natural strain rates. Finally, we discuss our results by evaluating vertical strength profiles and compare the implications thereof (e.g., the BDT depth) with available field data (e.g., the occurrence of local seismicity).

2. Methods

2.1. Sampling Material

Basalt samples were obtained from a block that was sourced from a quarry located in the western flank of Mt. Etna (Tanguy et al., 1997), as previously used in several studies (Benson et al., 2012; Fazio et al., 2017; Vinciguerra et al., 2005; Heap et al., 2009, 2018). The material investigated is a porphyritic alkali basalt with pyroxene, plagioclase, and olivine phenocrystals (largest ~2 mm) in a fine-sized groundmass of plagioclase, pyroxene, olivine, and magnetite (microlite size ~1 μm). Samples used in this study had a density of 2,850 kg/m^3 and a connected porosity of 5.40 ± 0.02% measured using a helium pycnometer (Micrometrics Accupyc 1330). Porosity is composed by both pores and microcracks (Vinciguerra et al., 2005), pores often comprised of space between microlites (i.e., minute crystals) where the ground mass is absent, and is similar to the diktytaxitic texture presented in Heap et al. (2018).

Representative samples of the thick carbonate successions of the Hyblean Plateau, believed to form Etna's deep basement (Catalano et al., 2004) were obtained from a quarry ~50 km south of Mt. Etna, near the town of Comiso (Branca et al., 2011). These samples originate from the same block as the samples that were used in Bakker et al. (2015). The samples consist of nearly 100% calcite (disregarding impurities, etc.) and have an isotropic crystallographic fabric, based on X-ray powder diffraction (XRD) and X-ray goniometry results. Porosity is identified as primary porosity, and no secondary porosity is observed (i.e., microcracks). Equivalent pore diameter is a few microns as evidenced by scanning electron microscope (SEM) imaging of undeformed material (Bakker, 2016). Starting porosity of the material was 8.70 ± 0.08% (connected porosity), measured by helium pycnometer as described above. The measured density of Comiso limestone was 2,468 kg/m^3.

2.2. Constant Strain Rate Tests ($T \geq 200\ °C$)

To determine the mechanical properties (elastic modulus, strength, and postpeak stress behavior) of Etna basalt samples, 13 triaxial deformation tests were performed with a Paterson apparatus installed at the Rock Deformation Laboratory, ETH Zürich. This machine is capable of deforming samples with a 10- to 15-mm diameter at confining pressures (P_c) up to 500 MPa and is equipped with an internal furnace capable of stable sample temperatures (T) of up to 1,200 °C. Experiments on Etna basalt were conducted on 10-mm diameter samples and ~25-mm length, (according to a 2.5:1 length to diameter ratio) as high axial strength was expected, particularly at low temperatures based on data from unconfined experiments (Benson et al., 2012). Samples are radially isolated from the confining medium (Argon gas) by a metallic jacket (copper [<700 °C] or iron [≥700 °C]; Bakker et al., 2015). Samples are coaxially mounted between ceramic pistons, ensuring a low thermal gradient across the sample axis (<2 °C/cm), as well as avoiding high temperatures at the top and bottom anvils. The load and displacement are measured by sensors located on an internally compensated piston, such that the differential load on the sample is directly measured (precision, 0.001 mm for displacement and 0.01 kN for load). Both sensors are connected to PID- (proportional integral derivative) controllers, allowing samples to be deformed in constant differential load mode, or constant displacement rate mode, which corresponds to constant (engineering) strain rate. In postprocessing, the displacement is corrected for deformation of the apparatus. Stresses are corrected for sample barreling and jacket contributions. Conditions used were $P_c = 50$ MPa of simulating relatively shallow subvolcanic settings, at a constant strain rate of $10^{-5}\ s^{-1}$, and with induced temperatures of 200 to 1,000 °C simulating proximity to magmatic bodies.

2.3. Low Temperature ($T \leq 200\ °C$) Friction Tests

At low temperatures both rock types deform by localized failure as suggested by UCS experiments on Etna basalt (Benson et al., 2012) and confined constant strain rate tests on Comiso limestone (Bakker et al., 2015). However, in field cases the edifice's strength will not be determined by intact rock but by the strength of existing faults, which are most likely weaker (e.g., Sibson, 1974). For this reason, the frictional strength was determined by continuous sliding after failure at a constant strain rate. Due to strain localization effects in the jacketing material when samples had failed, the contribution of the jacket to axial stress was too uncertain, such that axial load on the samples could not accurately be determined. Therefore, we used a conventional triaxial deformation apparatus installed in the Rock Mechanics Laboratory of the University of Portsmouth (e.g., Bakker et al., 2016; Fazio et al., 2017). This apparatus uses engineered FKM-B rubber jackets, which have a negligible influence on the mechanical data. Samples were deformed at $P_c = 30$ MPa until failure, with the subsequent sliding on the fault plane monitored in terms of stress and strain. After a sufficient amount of time (nominal 0.5% strain step), the confining pressure was increased stepwise, and a new steady state was established allowing a suite of axial (σ_1) and radial (i.e., $P_c =, \sigma_2 = \sigma_3$) stresses to be collected for friction coefficient analysis using classical Mohr-Coulomb theory. We note that temperature can have a significant effect on frictional properties (e.g., Pluymakers et al., 2016; Verberne et al., 2010) and therefore treat the results only as indicative values for the low-temperature range only. Friction testing at high temperature is required to further constrain the temperature dependence on friction coefficients.

2.4. Strain Rate Stepping Tests

For samples showing macroscopically ductile behavior, experiments were conducted where strain rate was varied during deformation in the Paterson apparatus. Based on previous tests (Bakker et al., 2015), low axial strength was expected, and therefore, 15×37.5 mm diameter × length samples were used. Several strain rate stepping tests were conducted at $500 < T < 800$ °C at 50 °C intervals. At each interval the strain rate test was performed as follows: A sample was initially deformed at a constant low rate (~$10^{-5}\ s^{-1}$) until yielding and achieving steady state flow (deformation at constant differential stress). After at least 5 min (corresponding to ~0.3–1.2% of finite strain, depending on the strain rate), the strain rate was increased by roughly $0.6 \times 10^{-5}\ s^{-1}$. This process was iterated until four pairs of differential stress and strain rates were obtained. The maximum strain rate did not exceed $10^{-4}\ s^{-1}$, so as to avoid exceeding the total strain limit (machine safety) of 12%. For all experiments, after reaching the maximum strain rate, the strain rate was then decreased stepwise to ensure that the effects caused by total accumulated strain were correctly accounted for (to check for a reversible process and no significant strain hardening effects).

3. Laboratory Results

3.1. Constant Strain Rate Tests

To compare temperature effects on deformation behavior of the two main lithologies that build up Mt. Etna's edifice and basement, we append existing constant strain rate experiments on Comiso limestone with new tests on Etna basalt at the same conditions. Samples of Etna basalt were deformed under 50 MPa of confining pressure and a constant strain rate of 10^{-5} s^{-1}, and the resulting stress-strain curves are shown in the left panel of Figure 1. All experiments started with a first linear increase with strain, (i.e., elastic region) after which the behavior would differ. Depending on the temperature of the experiment, the yield point (i.e., the point in the stress-strain curve at which deviation from elastic behavior and onset of permanent deformation occurs) was seen to vary. The results can roughly be grouped according to their stress-strain curve (Figure 1) as well as microstructure (Figure 2). For experiments at temperatures in the 200–700 °C range, samples deformed elastically up to a differential stress of around 600 MPa (~1% strain), and peak stresses between 650 and 800 MPa (at ~1.6% strain), with the experiment at 200 °C being on the weaker end, which we ascribe to sample variability. After reaching peak stress, a short period of weakening was then followed by a rapid drop in differential stress, accompanied by a sudden (uncontrollable) jump in strain: This was interpreted as the failure event. Jackets around the samples were not punctured, and samples were continuously deformed at the same strain rate until a steady state had occurred (i.e., no significant increase of differential stress with linearly increasing strain). Microstructural analysis of these samples after experimentation (Figure 2) showed a single fault plane at which the deformation had localized few splay cracks and subparallel fractures. The main fracture was 25–30° to the compression direction.

Experiments in the range between 800 and 975 °C exhibited yielding between 0.7% strain with peak stress in the range 400 and 500 MPa at approximately 1.5% strain. Postpeak stress was followed by strain weakening until reaching a steady state at stresses between 150 and 200 MPa. These differ from the experiments at lower temperatures not just by their lower peak stresses but also by the fact that there was a slow and controlled weakening phase after peak stress was reached, compared to the rapid (uncontrolled) sample failure at lower temperature, and subsequent reloading or increasing stress after failure (see Figure 1, left). In terms of microstructure, the samples of this group ($700 < T \leq 975$ °C) are characterized by a zone of anastomosing fractures, linking up into one shear zone with a width up to 500 μm (Figure 2c). At the highest temperature of 1,000 °C, a markedly different behavior is evident. Here there is no clear linear (elastic) trend, and no yield point is readily identified. The differential stress increased in a parabolic fashion until a peak stress of about 240 MPa at 1.3% strain. This was followed by a long period of weakening, to around 140 MPa at 5% strain. While the stress-strain curve suggests a "slow" brittle failure, the microstructure did not reveal a fault or a shear zone as with previous samples. Instead, we observed macroscopically distributed deformation, although minor fractures and cracks were observed (Figure 2d). No dominant mechanism can be distinguished, the plastic type deformation observed in the stress-strain curve is likely a combination of ductile mechanisms (e.g., dislocation creep) as well as cataclastic flow (indicated by minor fractures). However, this result does indicate that the combination of pressure, temperature, and strain rate conditions of this experiment are close to the BDT of Etna basalt.

Compared to unconfined experiments, ran at a similar temperature range (Benson et al., 2012), confined experiments reveal a marked degradation of strength between 700 and 800 °C, whereas in the unconfined case significant changes were suggested to happen above 950 °C (Benson et al., 2012). Our results suggest that the BDT for Etna basalt lies above 975 °C and close to 1,000 °C (at a strain rate of 10^{-5} s^{-1} and $P_c = 50$ MPa). However, up to at least 700 °C, Etna basalt deforms in similar manner to room temperature conditions. As temperatures within the basaltic edifice are not likely to exceed 700 °C, we consider the rheological behavior to be best captured by the frictional strength. To fully map out the BDT for Etna basalt would require experiments at higher temperatures, which is beyond the scope of this work as temperatures in the edifice are on average well below the BDT, with the exception of close proximity to intrusions (e.g., Castagna et al., 2018)

To compare with the contrasting basement lithology (Figure 1, right), we summarize the triaxial constant strain rate tests on dry Comiso limestone, presented by Bakker et al. (2015). These results suggest brittle behavior up to 400 °C at a strain rate of 10^{-5} s^{-1} and $P_c = 50$ MPa when considering total strain up to 10%, evidenced by localization and the sudden loss of load carrying capacity. Up to 400 °C it can be shown that
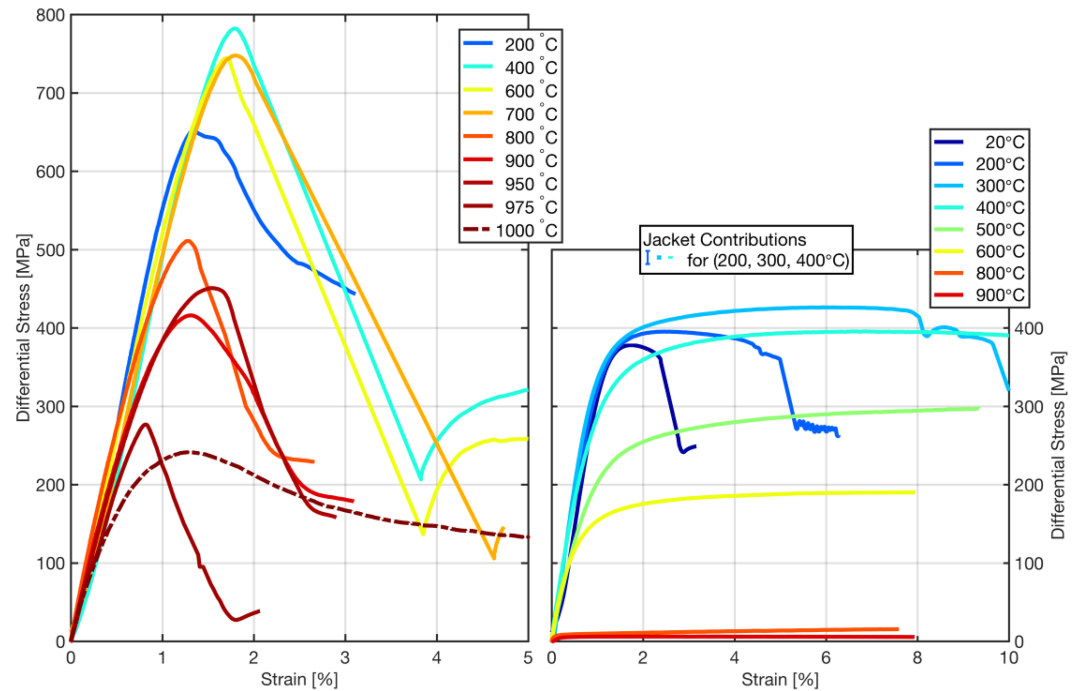
AGU
100
ADVANCING EARTH
AND SPACE SCIENCE

Journal of Geophysical Research: Solid Earth

10.1029/2019JB017399

Figure 1. Results from constant strain rate ($10^{-5}\,s^{-1}$) experiments at 50 MPa of confining pressure. The same color scale is used in both figures. Left, Etna basalt (this study); right, Comiso limestone for comparison (adapted from Bakker et al., 2015, to match the same color scale). Note that the differential stress is plotted on the same scale, but strain axes are different. Jacket contributions for Comiso limestone and Etna basalt are similar. Propagated measurement errors resulting from load and displacement data are less than depicted by the line thickness: 0.12 MPa in differential stress and 0.005% in strain for a 10×22 mm (diameter $\times$ length) sample.

the total strain at failure increases markedly (longer yielding period). With $T > 400\,°C$, it can be observed that overall sample strength decreases with temperature, indicating a deformation mechanism that is strongly dependent on temperature.

3.2. Room Temperature Friction Tests (Etna Basalt and Comiso Limestone)

As the experiments at high temperature proved unsuitable for the determination of friction coefficients, these were determined by running a different set of dedicated experiments at room temperature. Frictional strength was determined from postpeak continuous sliding on the produced fault planes for both rock types. Pairs of normal and shear stress were determined from parts of the stress-strain curves where steady state shearing occurred. These were then plotted in a Mohr-diagram and fitted with a linear line to determine the friction coefficient. The equation relating stresses is

$$\tau = C + \mu\sigma_n, \tag{1}$$

where μ is the coefficient of friction, C is a constant, and σ_n is the normal stress on the fault.

For Etna basalt we find a friction coefficient of $\mu = 0.704 \pm 0.010$ and $C = 23.35 \pm 0.50$ MPa. For Comiso limestone we find a friction coefficient of $\mu = 0.745 \pm 0.010$ and $C = 12.03 \pm 0.50$ MPa. Errors are determined by the propagation of instrument errors. Theoretically, the linear regression crosses the origin of the plot (i.e., no cohesion). However, our results do show some residual cohesion for both rock types, indicating continuous damaging of the main fault plane.

The friction coefficients presented here compare well with a friction coefficient of 0.85 for normal stresses below 200 MPa, commonly accepted for a wide range of rock types (Byerlee, 1978). Particularly for Etna basalt, our friction coefficient compares well to previous results such as $\mu = 0.79 \pm 0.21$, basalt (Schultz, 1993); $\mu = 0.68$, microgabbro (similar chemical composition; Violay et al., 2014); $\mu = 0.64$, Etna basalt (rotary shear experiments and static friction; from Violay, Gibert, et al., 2015). The frictional strength of Comiso limestone compares well to the calcite-rich fault gouges, $\mu = 0.7–0.8$ (Verberne et al., 2013).
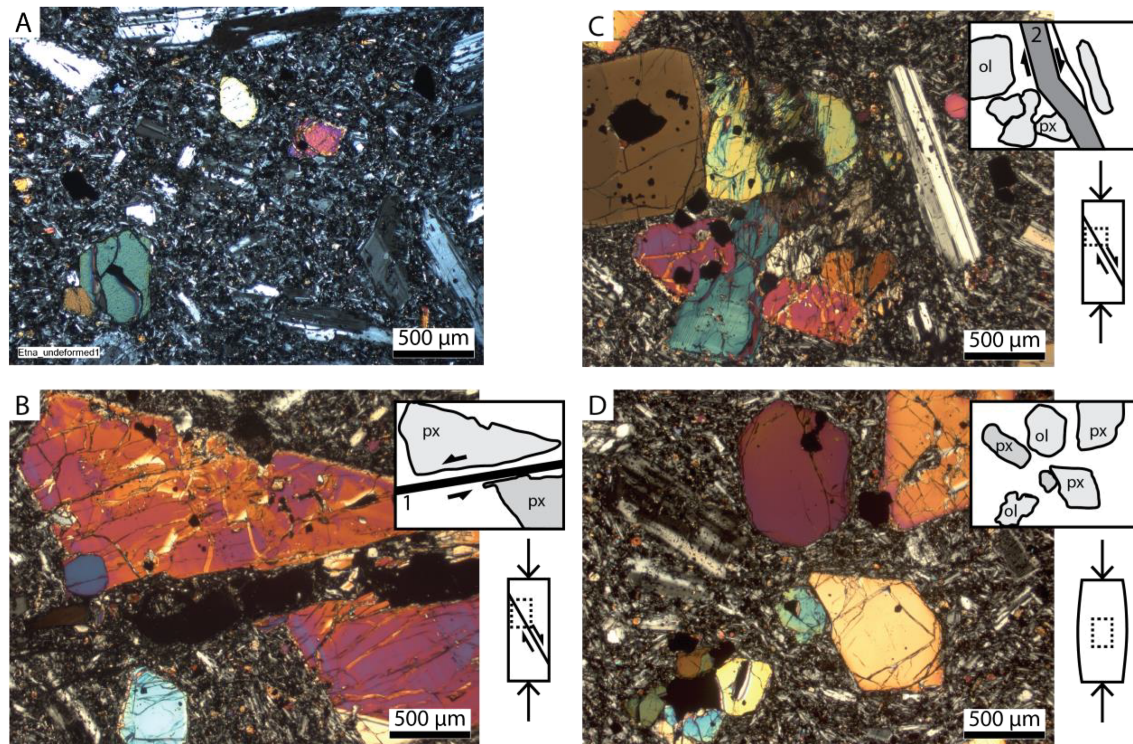
Figure 2. Microscope pictures of thin sections in cross-polarized transmitted light, observable phenocrysts: px (pyroxene) and ol (olivine). Panel (a) is the undeformed starting material; panel (b) shows sample material deformed at 600 °C where one fracture was observed (see inset, indicated by 1). Panel (c) was deformed at 800 °C and shows an anastomosing fracture type (see inset, indicated by 2). Finally, panel (d) illustrates sample deformed at 1,000 °C where no fracture was observed.

3.3. Strain Rate Stepping Tests (Comiso Limestone)

Experiments at constant strain rate on Etna basalt showed a macroscopically ductile response at $T > 975$ °C. Since Etna basalt occurs mostly in the top part of the volcanic edifice where temperatures are not as high, we did not evaluate the ductile behavior of Etna basalt further via the strain stepping method. However, for Comiso limestone with its BDT temperature at 350 °C (at a strain rate of 10^{-5} s^{-1}; Bakker et al., 2015), it is crucial to determine the ductile strength. Temperatures exceeding 350 °C are easily reached in volcanic basements (e.g., Flóvenz & Saemundsson, 1993) and in the case of Etna they are evidenced by fumarole-gas chemistry (e.g., Liotta et al., 2010).

Experiments were conducted within the strain rate range of $1–5 \times 10^{-5}$ s^{-1}. Overall, the decrease in the ductile strength with increasing temperature ranging from 350 MPa at 500 °C to just 40 MPa at 800 °C, at the same strain rate (2.2×10^{-5} s^{-1}; Figure 3), a similar decrease in magnitude over the same temperature range as observed from experiments ran at a strain rate of 10^{-5} s^{-1} (Bakker et al., 2015). In all cases, the increased strain rate yielded an increase in the differential stress that could be sustained, and this process was predominantly reversible. It is evident that the reversibility is only partial at the lower temperature range of these experiments. For example, the sequence at 500 °C shows a stress of approximately 350 MPa after lowering strain rate back to 1.8×10^{-5}, compared to approximately 320 MPa just before the initiation of the increase in strain rate. In comparison, the sequence at 800 °C ends and starts at a differential stress value of approximately 20 MPa with no observed difference, and the process is reversible. The partial reversibility at $T < 750$ °C, which is no longer observed at higher T, implies that deformation mechanisms within the experiment temperature range might have changed.

3.4. Data Fitting: Constitutive Laws for Deformation

For all experiments, increasing strain rates lead to a higher steady state differential stress and vice versa (Figure 3). At comparable strain rates, higher temperatures lead to lower steady state differential stresses.
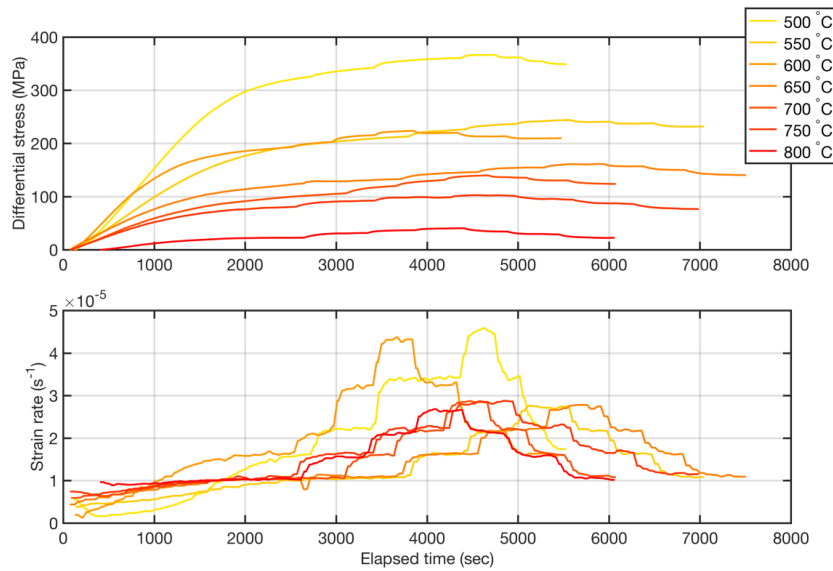
Figure 3. Differential stress (upper diagram) and strain rate (s^{-1}, lower diagram) plotted as a function of time for the strain rate stepping experiments conducted on Comiso limestone. Associated errors are smaller than the depicted line thickness (see also figure 1). The ductile strength decreases with temperature and increases with increasing strain rate.

From these data, we extracted triplets of differential stress, strain rate, and temperature at segments of steady state behavior and plotted these in three-dimensional space with axes: log (stress), log (strain rate), and "1/RT" (Figure 4). This allowed the data to be visualized and analyzed using an intracrystalline plasticity-type law as conducted by earlier work using limestone (e.g., Rutter, 1972; Schmid et al., 1977). This law has the general form

$$\dot{\varepsilon} = A_0 \cdot \sigma^n \cdot e^{-\frac{Q}{RT}}, \tag{2}$$

where $\dot{\varepsilon}$ is the strain rate (s^{-1}), A_0 is the pre-exponent factor (Pa^{-n}/s); σ is the differential stress (Pa); n the stress exponent ($\Delta\log(\text{Pa})/\Delta\log(\text{s}^{-1})$); Q the activation energy (kJ/mol); R the universal gas constant, 8.314 (J·mol^{-1}·K^{-1}); and T the absolute temperature (K).

To assess the material parameters n, Q, and A_0, a single regression step is applied following the method of Sotin and Poirier (1984; see the supporting information for details). Compared to conventional methods, this has the advantage that no singular parameter needs to be fixed or assumed prior to determining the other
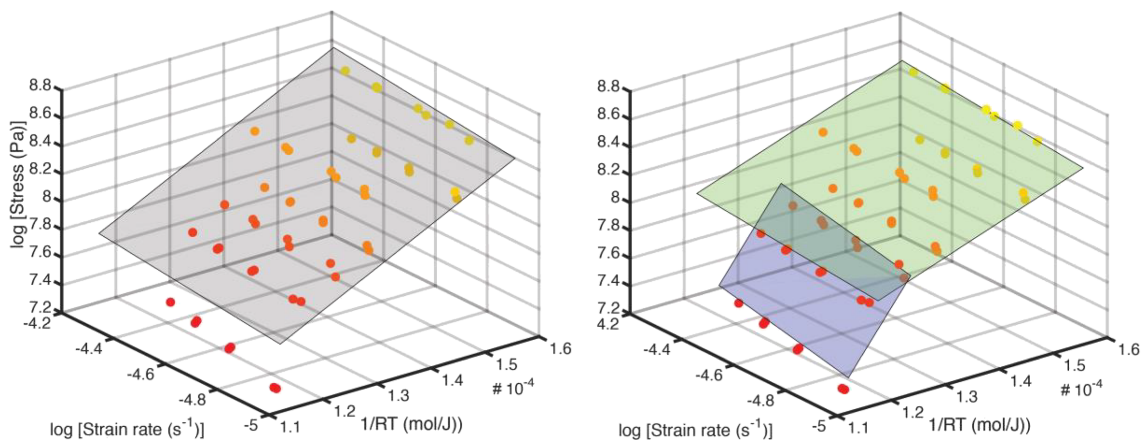

Figure 4. (a) Graphical representation of experimentally derived data points (spheres plotted in log [stress], log [strain rate], and 1/RT space) and best fit solution of equation (2), represented by a single plane; solution fit $r^2 = 0.84$. (b) Result of a best fit solution using two temperature ranges: 500–750 °C data (green) and 700–800 °C data (blue), solution fit $r^2 = 0.99$.
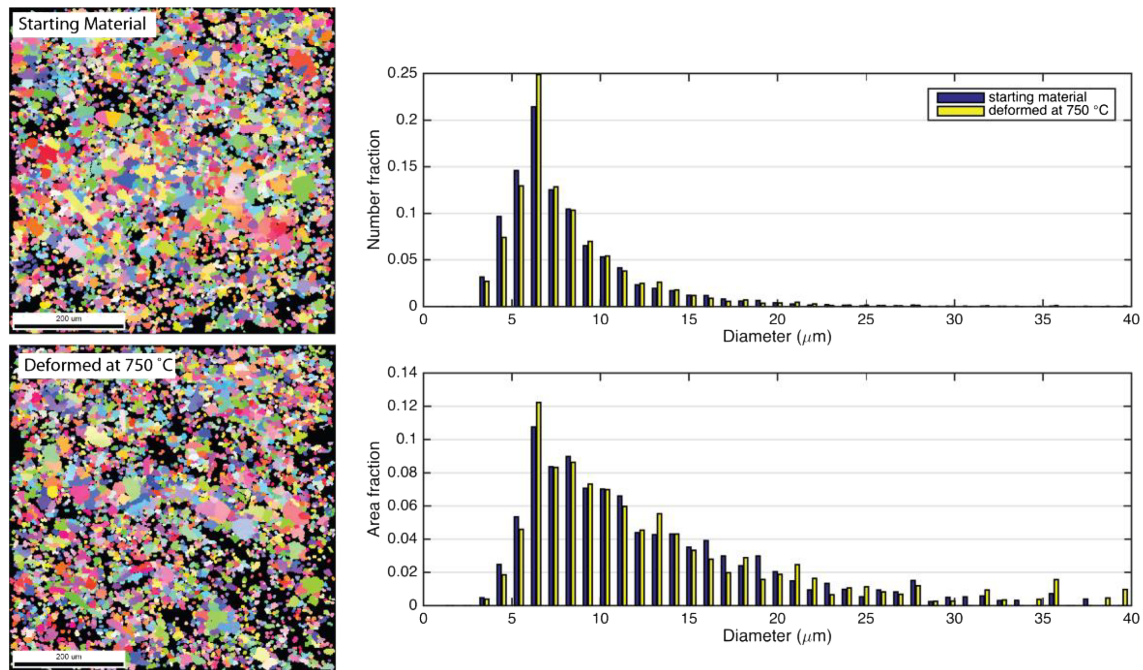
Figure 5. Electron back scatter diffraction analysis on the grain-size distribution. No grain-size reduction is evident when comparing starting materials (top, left) with sample material deformed at 750 °C (bottom left) with only macroscopic effects seen in hand specimen.

two. For example, conventionally one first determines the stress exponent and uses that value to determine Q and A_0 by means of linear regression in 2-D. Hereby, a significant error could potentially be introduced due to variability in values of the stress exponent. The approach chosen here (fitting three parameters in a single regression step) yields in a stress exponent of ~4.5, an activation energy of 202.2 kJ/mol, and a pre-exponential factor of $A_0 = 2.1 \times 10^{-30}$ Pa^{-n}/s, depicted by the gray plane in Figure 4.

While this solution offers reasonable results, yielding an r^2 of 0.84, it is clear that the data set features a prominent "break of slope" at temperatures between 700 and 750 °C—consistent with the previous observation of an implied variation in mechanism (the difference in strain hardening effect at high temperature). Previous work has also suggested that different deformation mechanisms may operate (e.g., Walker et al., 1990). To distinguish a dominating mechanism, the data were reinterpreted using two temperature regimes, consisting of a low-temperature fit with the 500–750 °C data (Figure 4b, green plane) and a high-temperature fit using the 700–800 °C data (Figure 4b, blue plane) based on an error analysis of the initial single plane fit. In the dual plane approach, the two fits share a temperature overlap to identify the temperature range over which one fitting regime becomes dominant. As shown comparing the two fits in Figure 4, the latter approach results in an improved fit and provides evidence that the deformation mechanism could have changed. This updated analysis reveals an excellent fit ($r^2 = 0.99$), with a low/medium temperature regime characterized by a stress exponent of ~5.3, a relatively low activation energy of 170.6 kJ/mol, and a pre-exponential factor of 2.57×10^{-39} Pa^{-n}/s and a high temperature regime characterized by a stress exponent of ~2.4, an activation energy of 293.4 kJ/mol, and a pre-exponential factor of 1.65×10^{-09} Pa^{-n}/s.

Here, we do not consider grain-size sensitive processes to be of significant importance as posttest microstructural analysis revealed no localization. Moreover, there were no indications of grain-size sensitive deformation or diffusion such as curvature of lobate grain boundaries, chemical zoning, or newly crystallized fine grain aggregates. Evidence for this came from electron back scatter diffraction technique allowing grain-size distribution, aspect ratio, and crystallographic preferred orientation to be quantitatively determined (Figure 5). Here, grain-size distribution of a sample deformed at 750 °C up to 10% strain was comparable to that of undeformed samples: The only deformation observed was at the sample scale, such as barreling. Grain-size sensitive mechanisms are not excluded by this but considered to be negligible within our

experimental results. Moreover, a drawback of using natural samples is that the grain size varies naturally and cannot be systematically controlled. Natural samples are also more likely to contain impurities, which have been shown to inhibit grain-size sensitive processes (e.g., Llana-Fúnez & Rutter, 2008; Rutter et al., 1994; Walker et al., 1990).

4. Discussion: A Strength Profile for Mt. Etna

With a strategy for data fitting established, a combined vertical strength profile for the rheology of the Mt. Etna system can be built up with a few assumptions that are discussed here. First, we assume that our laboratory results on Etna basalt is representative for the edifice, whereas the deep basement is represented by Comiso limestone. We acknowledge that our laboratory approach neglects to include the Appennine Maghrebian Chain (AMC) complexity. However, mechanical properties (Wiesmaier et al., 2015) measured for a suite of lithologies (quartzarenites, arenites, calcarenites, shales, cacirudites, and radiolarite-bearing limestones) representative of its variability revealed a behavior consistent with cohesive rocks and slightly weaker than Comiso Limestone, when compared at ambient pressure (e.g., UCS average around 50 MPa for the AMC lithologies and UCS around 100 MPa for Comiso limestone). Our generalized representation of the AMC also includes low-friction units, which are likely to develop sliding surfaces (Apuani et al., 2013; Nicolosi et al., 2014). These are more known as the sub-Etnean clays, which have been extensively mapped and occur only as a relatively thin layer (Branca et al., 2011). As we could not have direct measurements of these lithologies (significantly large variabilities and weathering effects prevented the collection of representative samples), we relied on material properties taken from the literature on similar rock types. The weak nature of the AMC is represented by treating the entire unit as a low-friction unit. This approach acknowledges that clay-rich layers are present within the AMC (e.g., Wiesmaier et al., 2015) and allows us to compare the strength of the AMC with the deeper (and therefore hotter) carbonates. Note also that carbonate strata present within the AMC can also be significant weakness at high temperatures (Heap et al., 2013; Mollo et al., 2013). While representing the mechanical behavior with a frictional law may not reflect the actual deformation mechanism, the resulting relatively low magnitude of strength is captured by the assumption.

The resulting strength envelope, per depth interval (Figure 6, right), follows the minima of the governing equations (i.e., weakest rheology). In addition, we assume that temperature depth follows a linear geothermal gradient (Figure 6, left). To acknowledge that geothermal gradients vary, we considered a reasonably wide range spanning 50 to 150 °C/km (common for volcanic systems; e.g., Flóvenz & Saemundsson, 1993). Lithostatic pressure with depth, $P(z)$ is calculated as the integral of the density, ρ_{lith} multiplied with the gravitational acceleration, g, across the depth range of interest (equation (3)), allowing the density to vary according to the lithology. We take a density of 2,850 kg/m^3 for Etna basalt, 2,468 kg/m^3 for Comiso limestone, and 2,400 kg/m^3 for AMC (Wiesmaier et al., 2015).

$$P(z) = \int_{base\ limestone}^{top\ basalt} \rho_{lith}(z) \cdot g \cdot dz \qquad (3)$$

For most crystalline and strong rock types, a typical strength profile would follow Byerlee's rule (Byerlee, 1978) for the upper crustal frictional strength (e.g., Kohlstedt et al., 1995). However, friction coefficients vary widely (Byerlee, 1978), particularly at shallow depths, due to a strong dependence on surface roughness and the presence of water/fluid pressurization (e.g., Burg & Schmalholz, 2008). The relation between shear and normal stress proposed by Byerlee (1978) is unsuitable here, as pore pressurization due to magmatic fluids and water infiltration are both ubiquitous at Mt. Etna (Giammanco et al., 1998). For a rigorous comparison of maximum stress in the frictional regime, we therefore consider both approaches (that of Sibson, 1974, depicted as friction law in Figure 6 and Byerlee, 1978, depicted as Byerlee's rule), presented together in Figure 6. Specifically, we apply a pore-to-lithostatic pressure ratio (λ) of 0.4, considered suitable for volcanic systems (Day, 1996). For the AMC horizon, we only consider the frictional strength as that is likely the weakest mechanism. We use a representative friction coefficient of $\mu = 0.2$, (Alparone et al., 2015) based on clay shearing experiments of Takahashi et al. (2007).

To account for a reasonable variation in friction coefficients, the friction coefficients are assumed to vary by ±0.1 with respect to the measured/inferred values. This range allows constructing upper and lower bounds
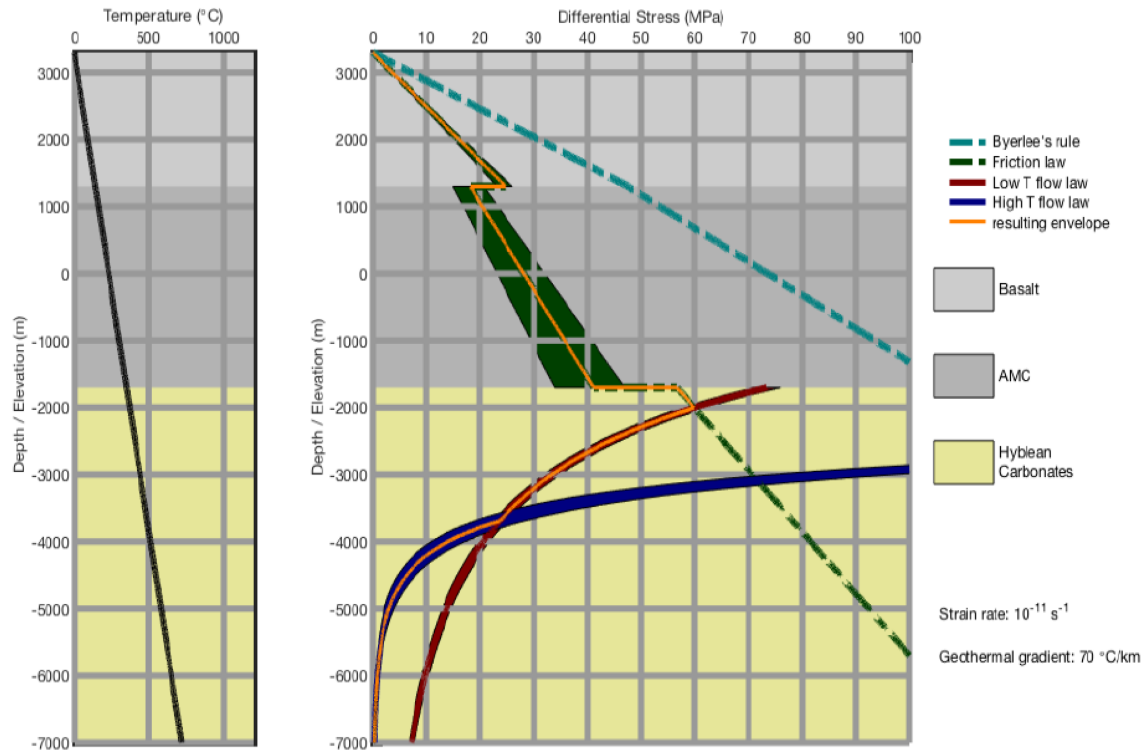
Figure 6. (Left) Our implied temperature change (geothermal gradient) with depth, for an assumed geothermal gradient of 70 °C/km. (Right) Applying this data with friction coefficient (dark green dashes) and material properties via equations (3) and (4) reveals several options for a strength profile for Mt. Etna. At shallow levels the Byerlee profile (light blue dashes) increases in a mostly linear dependence with depth to 1,000 m below sea level. Two ductile processes at low and high temperature are shown in dark red and dark blue solid lines, respectively, representing our experimental data. The overall envelope (thin orange line) takes into account the dominant mechanism as we descend, essentially the weakest strength of the available processes.

for the frictional strength. Such an error is an order of magnitude higher than the experimental error but is imposed to account for sample variability. Further uncertainty may also arise from the ductile flow laws; data are extrapolated from a relatively low range of magnitudes in terms of strain rates due to conventional laboratory constraints.

Overall, seismicity occurring at Mt. Etna is characterized by an prevailing strike-slip regime (e.g., Alparone et al., 2012; Bonanno et al., 2011). Brittle faulting of the volcano at shallow levels is likely dominated by normal faulting and, on volcanic edifices, is often dominated by "collapse" faulting or flank collapse (Harnett et al., 2018; Lagmay et al., 2000; Merle et al., 2001; Murray et al., 2018). At Mt. Etna volcano about 50% of earthquakes are shallow (<5 km b.m.s.l.) and mainly located in the structurally unstable eastern flank (Alparone et al., 2015; Patanè et al., 2004). Seismicity is present in a wide range of depths (*d*) down to 30 km, with intermediate events (5 < *d* < 12 km) and deeper seismicity (12 < *d* < 33 km) occurring on the western flank mainly (Sicali et al., 2014) and interpreted as related to the activation of regional tectonics enhancing magma transfer from the crust within the volcanic edifice (Patanè et al., 2004; Sicali et al., 2014). Overall the response of the volcanic edifice is brittle, as the vast majority of the seismicity occurs within the first 7 km of depth (e.g., Alparone et al., 2015). We therefore assume a normal mode of failure, for which the governing equation (based on Sibson, 1974) takes the form

$$\sigma_f = \frac{2P(z)\mu(1-\lambda)}{\sqrt{\mu^2+1}+\mu}, \tag{4}$$

where σ_f denotes the differential stress required to shear in a normal faulting regime (MPa), $P(z)$ is the lithostatic pressure (MPa), μ is the friction coefficient, and λ is the ratio between pore and lithostatic pressure. For ductile processes, equation (2) may be rewritten a:
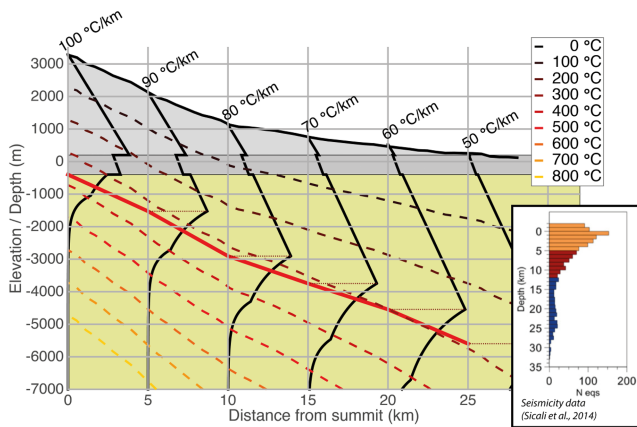
Figure 7. Change in the brittle-to-ductile deformation regime as forecast by our combined rheological model. The solid red line denotes the depth at which the transition projects to the surface, moving away from the summit vent. As distance from the summit vents increased, it is matched by a concomitant decrease in geothermal gradient. The inset shows earthquake distribution with depth around and underneath Mt. Etna. Data are from Sicali et al. (2014) and are color coded for depth range.

$$\sigma_d = \left[\frac{\dot{\varepsilon}}{A_0 e^{-Q/RT}} \right]^{\frac{1}{n}}, \qquad (5)$$

where σ_d is the differential stress required to deform the material by means of ductile flow at a given strain rate and temperature, applied according to the boundary conditions stated above.

The resulting strength envelope at each depth interval follows the minimum value of the resulting two expressions (3) or (4) above. As the application of any stress will result in a strain, and it is well known that strain rates at volcanoes can vary over several orders of magnitude in volcanic systems, we next explore a range between 10^{-14} s^{-1} (background tectonic strain rate; e.g., Karato, 2010) to 10^{-8} s^{-1} (rapid deformation during volcanic activity; e.g., Fournier, 1999). Fortunately, due to Mt. Etna's extensive Global Positioning System (GPS) network and years of continuous monitoring, strain rates could be inferred and allow for comparison with field data (seismicity). Neri et al. (2005) found a background strain rate of 8×10^{-14} s^{-1} using long Electronic Distance Measurements (EDM) measurements on three spots on the volcanic edifice, taken between different eruptive episodes. Figure 6 shows the rheological profile based a strain rate that is roughly in the middle of that range, as well as a moderate geothermal gradient of 70 °C/km. However, GPS-based measurements give background strain rates, which are slightly higher than those reported by Neri et al. (2005): at 2–5×10^{-13} s^{-1} (Bruno et al., 2012). We therefore employ a value of 10^{-13} s^{-1} as background strain rate for Mt. Etna when comparing with seismic data (see Figure 7).

Although the approach above suffers from "sharp corner" issues—particularly at approximately 2,000 m BSL (below sea level) where the friction dominated rheology transitions to the low temperature flow law—some verification of the approach comes from comparing the predicted depth of the BDT with seismicity, as the BDT may be considered the depth limit of seismicity (e.g., Scholz, 1988; Violay, Di Toro, et al., 2015). Seismicity in and around the Mt. Etna region is generally shallow and focused around the summit and the unstable eastern flank. These seismic events are associated to volcanic processes (Alparone et al., 2015). However, comparing earthquake foci in between volcanic episodes away from the volcano shallow dynamics (Sicali et al., 2014; Figure 7 inset), we show a good correlation with the BDT that we predict based on our constitutive laws, assuming a decreasing geothermal gradient with distance from the main summit vents. The primary transition from brittle to ductile (and therefore likely to result in a decrease in seismicity) moves from 2–3 km BSL at 80–90 °C/km up to some 5 km from the summit, to some 10 km BSL at 25 km from the summit.

5. Conclusion

We have investigated the rheological behavior of two main lithologies, which dominate edifice stability: Etna basalt representing the volcanic edifice and Comiso limestone as the carbonate basement. The mechanical strength is investigated in terms of pressure, temperature, and strain rate. We find that the edifice is best represented by a friction type flow law, which is applicable up to at least 700 °C, with a friction coefficient of 0.704. The carbonate basement of Mt. Etna is most likely at a temperature sufficient that ductile processes determine the strength. For Comiso limestone, representative for the deep part of the basement, we find that a single fit cannot adequately capture the measured rheology and instead a dual-fit type flow law is needed due to the underlying deformation mechanisms, modeled to general intracrystalline plasticity type flow laws. These are characterized by a low/medium temperature regime with $n = 5.3$; $Q = 170.6$ kJ/mol; and $A_0 = 2.57 \times 10^{-39}$ Pa^{-n}/s; and a high temperature regime with $n = 2.4$, $Q = 293.4$ kJ/mol, and $A_0 = 1.65 \times 10^{-09}$ Pa^{-n}/s.

To test the validity of our constitutive laws, we have built an analytical model represented by a strength profile where the effects of temperature, pressure, and strain rate may be varied. Our strength profile is able to explain the expected significant weakness in the basement of Mt. Etna. Moreover, our prediction of the BDT depth qualitatively corresponds well to the observed seismicity, further suggesting that the brittle behavior

ceases below this depth in intraeruptive periods. With these types of new laboratory data, numerical modeling approaches, used to better understand the basement processes, can now be improved by the addition of realistic material properties and may in turn lead to a better understanding of edifice stability at Mt. Etna, and volcanoes with carbonate basements in general.

References

Alparone, S., Barberi, G., Cocina, O., Giampiccolo, E., Musumeci, C., & Patanè, D. (2012). Intrusive mechanism of the 2008-2009 Mt. Etna eruption: Constraints by tomographic images and stress tensor analysis. *Journal of Volcanology and Geothermal Research*, *229-230*, 50–63. https://doi.org/10.1016/j.jvolgeores.2012.04.001

Alparone, S., Maiolino, V., Mostaccio, A., Scaltrito, A., Ursino, A., Barberi, G., et al. (2015). Instrumental seismic catalogue of Mt. Etna earthquakes (Sicily, Italy): Ten years (2000-2010) of instrumental recordings. *Annales de Geophysique*, *58*(4). https://doi.org/10.4401/ag-6591

Apuani, T., Corazzato, C., Merri, A., & Tibaldi, A. (2013). Understanding Etna flank instability through numerical models. *Journal of Volcanology and Geothermal Research*, *251*, 112–126. https://doi.org/10.1016/j.jvolgeores.2012.06.015

Bakker, R. R. (2016). *Understanding basement processes in sub-volcanic settings by laboratory measurements*. Zürich, Switzerland: ETH Zürich.

Bakker, R. R., Fazio, M., Benson, P. M., Hess, K.-U., & Dingwell, D. B. (2016). The propagation and seismicity of dyke injection, new experimental evidence. *Geophysical Research Letters*, *43*, 1876–1883. https://doi.org/10.1002/2015GL066852

Bakker, R. R., Violay, M. E. S., Benson, P. M., & Vinciguerra, S. C. (2015). Ductile flow in sub-volcanic carbonate basement as the main control for edifice stability: New experimental insights. *Earth and Planetary Science Letters*, *430*, 533–541. https://doi.org/10.1016/j.epsl.2015.08.017

Benson, P. M., Heap, M. J., Lavallée, Y., Flaws, A., Hess, K. U., Selvadurai, A. P. S., et al. (2012). Laboratory simulations of tensile fracture development in a volcanic conduit via cyclic magma pressurisation. *Earth and Planetary Science Letters*, *349-350*, 231–239. https://doi.org/10.1016/j.epsl.2012.07.003

Benson, P. M., Thompson, B. D., Meredith, P. G., Vinciguerra, S., & Young, R. P. (2007). Imaging slow failure in triaxially deformed Etna basalt using 3D acoustic-emission location and X-ray computed tomography. *Geophysical Research Letters*, *34*, L03303. https://doi.org/10.1029/2006GL028721

Bonanno, A., Palano, M., Privitera, E., Gresta, S., & Puglisi, G. (2011). Magma intrusion mechanisms and redistribution of seismogenic stress at Mt. Etna volcano (1997-1998). *Terra Nova*, *23*(5), 339–348. https://doi.org/10.1111/j.1365-3121.2011.01019.x

Borgia, A., Ferrari, L., & Pasquarè, G. (1992). Importance of gravitational spreading in the tectonic and volcanic\nevolution of Mount Etna. *Nature*, *357*(6375), 231–235. https://doi.org/10.1038/357231a0

Branca, S., Coltelli, M., Groppelli, G., & Lentini, F. (2011). Geological map of Etna volcano, 1:50,000 scale. *Italian Journal of Geosciences*, *130*(3), 265–291. https://doi.org/10.3301/IJG.2011.15

Branca, S., & Ferrara, V. (2013). The morphostructural setting of Mount Etna sedimentary basement (Italy): Implications for the geometry and volume of the volcano and its flank instability. *Tectonophysics*, *586*, 46–64. https://doi.org/10.1016/j.tecto.2012.11.011

Bruno, V., Mattia, M., Aloisi, M., Palano, M., Cannavò, F., & Holt, W. E. (2012). Ground deformations and volcanic processes as imaged by CGPS data at Mt. Etna (Italy) between 2003 and 2008. *Journal of Geophysical Research*, *117*, B07208. https://doi.org/10.1029/2011JB009114

Burg, J.-P., & Schmalholz, S. M. (2008). Viscous heating allows thrusting to overcome crustal-scale buckling: Numerical investigation with application to the Himalayan syntaxes. *Earth and Planetary Science Letters*, *274*(1–2), 189–203. https://doi.org/10.1016/j.epsl.2008.07.022

Byerlee, J. (1978). Friction of rocks. *Pure and Applied Geophysics*, *116*(4–5), 615–626. https://doi.org/10.1007/BF00876528

Castagna, A., Ougier-Simonin, A., Benson, P. M., Browning, J., Walker, R. J., Fazio, M., & Vinciguerra, S. (2018). Thermal damage and pore pressure effects on brittle-ductile transition of Comiso limestone. *Journal of Geophysical Research: Solid Earth*, *123*, 7644–7660. https://doi.org/10.1029/2017JB015105

Catalano, S., Torrisi, S., & Ferlito, C. (2004). The relationship between Late Quaternary deformation and volcanism of Mt. Etna (eastern Sicily): New evidence from the sedimentary substratum in the Catania region. *Journal of Volcanology and Geothermal Research*, *132*(4), 311–334. https://doi.org/10.1016/S0377-0273(03)00433-5

Chadwick, J. P., Troll, V. R., Ginibre, C., Morgan, D., Gertisser, R., Waight, T. E., & Davidson, J. P. (2007). Carbonate assimilation at Merapi Volcano, Java, Indonesia: Insights from crystal isotope stratigraphy. *Journal of Petrology*, *48*(9), 1793–1812. https://doi.org/10.1093/petrology/egm038

Day, S. J. (1996). Hydrothermal pore fluid pressure and the stability of porous, permeable volcanoes. *Geological Society of London, Special Publication*, *110*(1), 77–93. https://doi.org/10.1144/GSL.SP.1996.110.01.06

Fazio, M., Benson, P. M., & Vinciguerra, S. (2017). On the generation mechanisms of fluid-driven seismic signals related to volcano-tectonics. *Geophysical Research Letters*, *44*, 734–742. https://doi.org/10.1002/2016GL070919

Flóvenz, Ó. G., & Saemundsson, K. (1993). Heat flow and geothermal processes in Iceland. *Tectonophysics*, *225*(1–2), 123–138. https://doi.org/10.1016/0040-1951(93)90253-G

Fournier, R. O. (1999). Hydrothermal processes related to movement of fluid from plastic into brittle rock in the magmatic-epithermal environment. *Economic Geology*, *94*(8), 1193–1211. https://doi.org/10.2113/gsecongeo.94.8.1193

Giammanco, S., Inguaggiato, S., & Valenza, M. (1998). Soil and fumarole gases of Mount Etna: Geochemistry and relations with volcanic activity. *Journal of Volcanology and Geothermal Research*, *81*(3–4), 297–310. https://doi.org/10.1016/S0377-0273(98)00012-2

Harnett, C. E., Benson, P. M., Rowley, P., & Fazio, M. (2018). Fracture and damage localization in volcanic edifice rocks from El Hierro, Stromboli and Tenerife. *Scientific Reports*, *8*(1), 1942–1948. https://doi.org/10.1038/s41598-018-20442-w

Heap, M. J., Baud, P., Meredith, P. G., Vinciguerra, S., Bell, A. F., & Main, I. G. (2011). Brittle creep in basalt and its application to time-dependent volcano deformation. *Earth and Planetary Science Letters*, *307*(1–2), 71–82. https://doi.org/10.1016/j.epsl.2011.04.035

Heap, M. J., Farquharson, J. I., Baud, P., Lavallée, Y., & Reuschlé, T. (2015). Fracture and compaction of andesite in a volcanic edifice. *Bulletin of Volcanology*, *77*(6), 55. https://doi.org/10.1007/s00445-015-0938-7

Heap, M. J., Mollo, S., Vinciguerra, S., Lavallée, Y., Hess, K. U., Dingwell, D. B., et al. (2013). Thermal weakening of the carbonate basement under Mt. Etna volcano (Italy): Implications for volcano instability. *Journal of Volcanology and Geothermal Research*, *250*, 42–60. https://doi.org/10.1016/j.jvolgeores.2012.10.004

Heap, M. J., Reuschlé, T., Farquharson, J. I., & Baud, P. (2018). Permeability of volcanic rocks to gas and water. *Journal of Volcanology and Geothermal Research*, *354*, 29–38. https://doi.org/10.1016/j.jvolgeores.2018.02.002

Heap, M. J., Vinciguerra, S., & Meredith, P. G. (2009). The evolution of elastic moduli with increasing crack damage during cyclic stressing of a basalt from Mt. Etna volcano. *Tectonophysics*, *471*(1–2), 153–160. https://doi.org/10.1016/j.tecto.2008.10.004

Iacono-Marziano, G., Gaillard, F., Scaillet, B., Pichavant, M., & Chiodini, G. (2009). Role of non-mantle CO2 in the dynamics of volcano degassing: The Mount Vesuvius example. *Geology*, *37*(4), 319–322. https://doi.org/10.1130/G25446A.1

Karato, S. I. (2010). Rheology of the Earth's mantle: A historical review. *Gondwana Research*, *18*(1), 17–45. https://doi.org/10.1016/j.gr.2010.03.004

Kohlstedt, D. L., Evans, B., & Mackwell, S. J. (1995). Strength of the lithosphere: Constraints imposed by laboratory experiments. *Journal of Geophysical Research*, *100*(B9), 17,587–17,602. https://doi.org/10.1029/95JB01460

Lagmay, A. M. F., van Wyk De Vries, B., Kerle, N., & Pyle, D. M. (2000). Volcano instability induced by strike-slip faulting. *Bulletin of Volcanology*, *62*(4–5), 331–346. https://doi.org/10.1007/s004450000103

Liotta, M., Paonita, A., Caracausi, A., Martelli, M., Rizzo, A., & Favara, R. (2010). Hydrothermal processes governing the geochemistry of the crater fumaroles at Mount Etna volcano (Italy). *Chemical Geology*, *278*(1–2), 92–104. https://doi.org/10.1016/j.chemgeo.2010.09.004

Llana-Fúnez, S., & Rutter, E. H. (2008). Strain localization in direct shear experiments on Solnhofen limestone at high temperature—Effects of transpression. *Journal of Structural Geology*, *30*(11), 1372–1382. https://doi.org/10.1016/j.jsg.2008.07.004

Merle, O., Vidal, N., & van Wyk de Vries, B. (2001). Experiments on vertical basement fault reactivation below volcanoes. *Journal of Geophysical Research*, *106*(B2), 2153–2162. https://doi.org/10.1029/2000JB900352

Mollo, S., Heap, M. J., Dingwell, D. B., Hess, K. U., Iezzi, G., Masotta, M., et al. (2013). Decarbonation and thermal microcracking under magmatic P-T-fco2 conditions: The role of skarn substrata in promoting volcanic instability. *Geophysical Journal International*, *195*(1), 369–380. https://doi.org/10.1093/gji/ggt265

Mollo, S., Heap, M. J., Iezzi, G., Hess, K. U., Scarlato, P., & Dingwell, D. B. (2012). Volcanic edifice weakening via decarbonation: A self-limiting process? *Geophysical Research Letters*, *39*, L15307. https://doi.org/10.1029/2012GL052613

Mollo, S., Vinciguerra, S., Iezzi, G., Iarocci, A., Scarlato, P., Heap, M. J., & Dingwell, D. B. (2011). Volcanic edifice weakening via devolatilization reactions. *Geophysical Journal International*, *186*(3), 1073–1077. https://doi.org/10.1111/j.1365-246X.2011.05097.x

Murray, J. B., Van Wyk De Vries, B., Pitty, A., Sargent, P., & Wooller, L. (2018). Gravitational sliding of the MtEtna massif along a sloping basement. *Bulletin of Volcanology*, *80*, 40.

Neri, M., Acocella, V., Behncke, B., Maiolino, V., Ursino, A., & Velardita, R. (2005). Contrasting triggering mechanisms of the 2001 and 2002-2003 eruptions of Mount Etna (Italy). *Journal of Volcanology and Geothermal Research*, *144*(1-4 SPEC. ISS), 235–255. https://doi.org/10.1016/j.jvolgeores.2004.11.025

Nicolosi, I., Caracciolo, F. D., Branca, S., Ventura, G., & Chiappini, M. (2014). Volcanic conduit migration over a basement landslide at Mount Etna (Italy). *Scientific Reports*, *4*(1), 5293. https://doi.org/10.1038/srep05293

Palano, M. (2016). Episodic slow slip events and seaward flank motion at Mt. Etna volcano (Italy). *Journal of Volcanology and Geothermal Research*, *324*, 8–14. https://doi.org/10.1016/j.jvolgeores.2016.05.010

Patanè, D., Cocina, O., Falsaperla, S., Privitera, E., & Spampinato, S. (2004). Mt. Etna volcano: A seismological framework. In *Mt. Etna: Volcano Laboratory* (pp. 147–165). Washington, DC: American Geophysical Union (AGU).

Pluymakers, A. M. H., Niemeijer, A. R., & Spiers, C. J. (2016). Frictional properties of simulated anhydrite-dolomite fault gouge and implications for seismogenic potential. *Journal of Structural Geology*, *84*, 31–46. https://doi.org/10.1016/j.jsg.2015.11.008

Poland, M. P., Peltier, A., Bonforte, A., & Puglisi, G. (2017). The spectrum of persistent volcanic flank instability: A review and proposed framework based on Kīlauea, Piton de la Fournaise, and Etna. *Journal of Volcanology and Geothermal Research*, *339*, 63–80. https://doi.org/10.1016/j.jvolgeores.2017.05.004

Rutter, E. H. (1972). The effects of strain-rate changes on the strength and ductility of Solenhofen limestone at low temperatures and confining pressures. *International Journal of Rock Mechanics and Mining Science and Geomechanics Abstracts*, *9*(2), 183–189. https://doi.org/10.1016/0148-9062(72)90020-4

Rutter, E. H. (1986). On the nomenclature of mode of failure transitions in rocks. *Tectonophysics*, *122*(3–4), 381–387. https://doi.org/10.1016/0040-1951(86)90153-8

Rutter, E. H., Casey, M., & Burlini, L. (1994). Preferred crystallographic orientation development during the plastic and superplastic flow of calcite rocks. *Journal of Structural Geology*, *16*(10), 1431–1446. https://doi.org/10.1016/0191-8141(94)90007-8

Schmid, S. M., Boland, J. N., & Paterson, M. S. (1977). Superplastic flow in finegrained limestone. *Tectonophysics*, *43*(3–4), 257–291. https://doi.org/10.1016/0040-1951(77)90120-2

Scholz, C. H. (1988). The brittle-plastic transition and the depth of seismic faulting. *Geologische Rundschau*, *77*(1), 319–328. https://doi.org/10.1007/BF01848693

Schultz, R. a. (1993). Brittle strength of basaltic rock masses with applications to Venus. *Journal of Geophysical Research*, *98*(E6), 10883. https://doi.org/10.1029/93JE00691

Sibson, R. H. (1974). Frictional constraints on thrust, wrench and normal faults. *Nature*, *249*(5457), 542–544. https://doi.org/10.1038/249542a0

Sicali, S., Barbano, M. S., D'Amico, S., & Azzaro, R. (2014). Characterization of seismicity at Mt. Etna volcano (Italy) by inter-event time distribution. *Journal of Volcanology and Geothermal Research*, *270*, 1–9. https://doi.org/10.1016/j.jvolgeores.2013.11.011

Sotin, C., & Poirier, J. P. (1984). Analysis of high-temperature creep experiments by generalized nonlinear inversion. *Mechanics of Materials*, *3*(4), 311–317. https://doi.org/10.1016/0167-6636(84)90031-0

Takahashi, M., Mizoguchi, K., Kitamura, K., & Masuda, K. (2007). Effects of clay content on the frictional strength and fluid transport property of faults. *Journal of Geophysical Research*, *112*, B08206. https://doi.org/10.1029/2006JB004678

Tanguy, J.-C., Condomines, M., & Kieffer, G. (1997). Evolution of the Mount Etna magma: Constraints on the present feeding system and eruptive mechanism. *Journal of Volcanology and Geothermal Research*, *75*(3–4), 221–250. https://doi.org/10.1016/S0377-0273(96)00065-0

Tibaldi, A., & Groppelli, G. (2002). Volcano-tectonic activity along structures of the unstable NE flank of Mt. Etna (Italy) and their possible origin. *Journal of Volcanology and Geothermal Research*, *115*(3–4), 277–302. https://doi.org/10.1016/S0377-0273(01)00305-5

van Wyk de Vries, B., & Borgia, A. (1996). The role of basement in volcano deformation. *Geological Society of London, Special Publication*, *110*(1), 95–110. https://doi.org/10.1144/GSL.SP.1996.110.01.07

van Wyk de Vries, B., & Francis, P. W. (1997). Catastrophic collapse at stratovolcanoes induced by gradual volcano spreading. *Nature*, *387*(6631), 387–390. https://doi.org/10.1038/387387a0

Verberne, B. A., He, C., & Spiers, C. J. (2010). Frictional properties of sedimentary rocks and natural fault gouge from the Longmen Shan fault zone, Sichuan, China. *Bulletin of the Seismological Society of America*, *100*(5 B), 2767–2790. https://doi.org/10.1785/0120090287

Verberne, B. A., Spiers, C. J., Niemeijer, A. R., De Bresser, J. H. P., De Winter, D. A. M., & Plümper, O. (2013). Frictional properties and microstructure of calcite-rich fault gouges sheared at sub-seismic sliding velocities. *Pure and Applied Geophysics*, *171*(10), 2617–2640. https://doi.org/10.1007/s00024-013-0760-0

Vinciguerra, S., Trovato, C., Meredith, P. G., & Benson, P. M. (2005). Relating seismic velocities, thermal cracking and permeability in Mt. Etna and Iceland basalts. *International Journal of Rock Mechanics and Mining Sciences*, *42*(7-8 SPEC. ISS), 900–910. https://doi.org/10.1016/j.ijrmms.2005.05.022

Violay, M., di Toro, G., Nielsen, S., Spagnuolo, E., & Burg, J. P. (2015). Thermo-mechanical pressurization of experimental faults in cohesive rocks during seismic slip. *Earth and Planetary Science Letters*, *429*, 1–10. https://doi.org/10.1016/j.epsl.2015.07.054

Violay, M., Gibert, B., Mainprice, D., & Burg, J.-P. (2015). Brittle versus ductile deformation as the main control of the deep fluid circulation in oceanic crust. *Geophysical Research Letters*, *42*, 2767–2773. https://doi.org/10.1002/2015GL063437

Violay, M., Nielsen, S., Gibert, B., Spagnuolo, E., Cavallo, A., Azais, P., et al. (2014). Effect of water on the frictional behavior of cohesive rocks during earthquakes. *Geology*, *42*(1), 27–30. https://doi.org/10.1130/G34916.1

Walker, A., Rutter, E. H., & Brodie, K. H. (1990). Experimental study of grain-size sensitive flow of synthetic, hot-pressed calcite rocks. *Geological Society of London, Special Publication*, *54*(1), 259–284. https://doi.org/10.1144/GSL.SP.1990.054.01.24

Wiesmaier, S., Heap, M. J., Branca, S., Gilg, H. A., Kueppers, U., Hess, K.-U., et al. (2015). Variability in composition and physical properties of the sedimentary basement of Mt Etna, Italy. *Journal of Volcanology and Geothermal Research*, *302*, 102–116. https://doi.org/10.1016/j.jvolgeores.2015.06.011